JOURNAL OF PROPULSION AND POWER
Vol. 18, No. 5, September–October 2002

# Effect of Integration of Scramjet into Airframe on Engine Performance and Payload

Daisuke Akihisa*
*Tohoku University, Aoba-ku, Sendai, Miyagi 980-8579, Japan*
Takeshi Kanda,† Kouichiro Tani,‡ and Kenji Kudo‡
*National Aerospace Laboratory of Japan, Kakuda, Miyagi 981-1525, Japan*
and
Goro Masuya§
*Tohoku University, Aoba-ku, Sendai, Miyagi 980-8579, Japan*

**There are three typical configurations for integrating the scramjet into the airframe of aerospace planes: 1) The whole engine is on the windward ramp surface of the airframe. 2) The engine is located downstream of the forebody ramp where the surface of the airframe is parallel to the airframe axis. 3) The inlet entrance is on the ramp surface with the following engine parts parallel to the airframe axis. To examine the effects of integration on the engine performance, several types of the inlet models were tested in a wind tunnel, and simulations of the scramjet engine and the flight of the aerospace plane were conducted. The experimental results showed that the first and the third configurations showed better mass capture. In the second configuration, the precompression effect was neutralized by the expansion fan from the corner of the downstream end of the ramp. All configurations showed similar levels for kinetic energy efficiency. The simulation based on the experimental results showed that the third configuration produced the best engine thrust and the least airframe drag. In the second configuration, however, the engine could not produce sufficient thrust. Thus, it is recommended that the inlet should be located on the windward ramp surface of the vehicle to capture the precompressed air and the following engine components should be parallel to the airframe axis to reduce the cowl drag and to increase the thrust of the external nozzle.**

## Nomenclature

| | | |
|---|---|---|
| $A$ | = | area |
| $C_F$ | = | thrust coefficient |
| $M$ | = | Mach number |
| $P$ | = | pressure |
| $\alpha$ | = | ramp angle or inclined angle of the top wall in the experiments |
| $\delta$ | = | boundary-layer thickness at 99% of the primary flow velocity |
| $\eta$ | = | efficiency |
| $\xi$ | = | ratio of averaged top wall pressure in isolator to freestream pressure |

*Subscripts*

| | | |
|---|---|---|
| all | = | total thrust with windward-surface airframe drag, engine thrust, and external-nozzle thrust |
| inlet | = | performance of inlet itself excluding the precompression effect |
| KE | = | kinetic energy |
| Pt | = | total pressure |
| ref | = | freestream reference condition in the experiments, that is, inclusion of a boundary layer on the plate and no inclination of top wall plate |
| $t$ | = | stagnation condition |
| total | = | inlet performance with precompression effect |
| $w$ | = | wall |
| 0 | = | wind-tunnel reservoir condition |
| 1 | = | at the inlet entrance |
| 2 | = | in the isolator |
| $\infty$ | = | freestream, flight condition |

Presented as Paper 2000-0619 at the AIAA 38th Aerospace Sciences Meeting and Exhibit, Reno, NV, 10–13 January 2000; received 1 November 2000; revision received 15 January 2002; accepted for publication 14 February 2002. 

*Graduate Student, Department of Aeronautics and Space Engineering; currently Engineer, Higashi-fuji Technical Center, Toyota Motor Corporation, Susono, Shizuoka 410-1193, Japan.

†Leader, Combined Cycle Engine System Group, Ramjet Propulsion Research Center. Senior Member AIAA.

‡Senior Researcher, Ramjet Propulsion Research Center.

§Professor, Department of Aeronautics and Space Engineering. Senior Member AIAA.

## Introduction

A SCRAMJET engine has high-performance potential at hypersonic flight of aerospace planes and hypersonic aircrafts. Integration of the engine into the airframe is beneficial because the forebody and the aftbody of the vehicle perform as a precompression stage and an external expansion stage, respectively.[1] In the airframe–engine integrated compression system, one or several oblique shock waves from the windward surface of the airframe are used for external compression. Several types of airframe–engine integration have been proposed and schematically illustrated in journal articles, technical papers, and textbooks. They can be categorized into the following three configurations for engine-mounting location.

1) For type a (Fig. 1a), the entire engine is attached to the ramp of the airframe, and the side view of the undersurface of the airframe forms a triangle or a flat plate.[1–4] In some cases, the engine is attached to the horizontal undersurface of the airframe, but with the attack angle, the undersurface practically works as a ramp. The airframe aft surface downstream of the engine works as an external nozzle. The axis of the engine is straight.

2) For type b (Fig. 1b), the side view of the undersurface of the airframe forms a trapezoid or a triangle. The engine is attached downstream of the ramp, where the surface is parallel to the airframe-axis.[5–8]

3) For type c (Fig. 1c), the side view of the undersurface of the airframe also forms a trapezoid, and the engine straddles over the

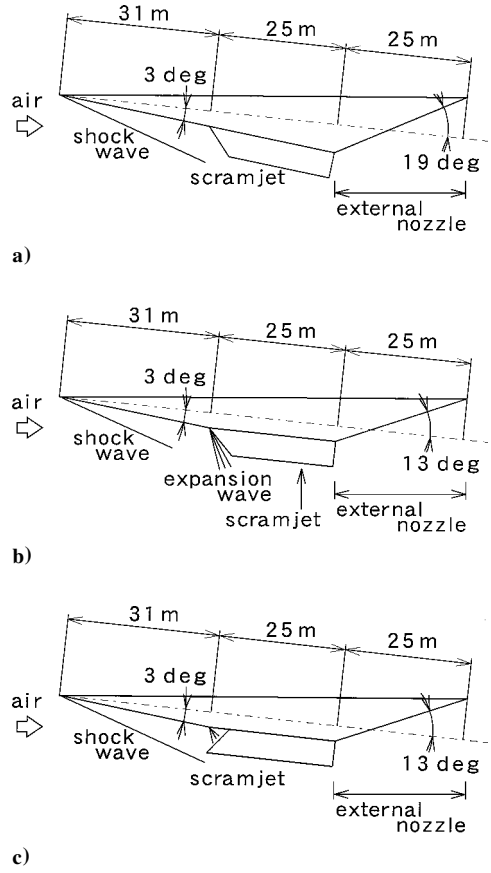


**Fig. 1 Vehicle configuration models for performance calculation: a) side view of type a, engine integrated on the ramp of the airframe; b) side view of type b, engine attached downstream of the rear corner of the airframe ramp; c) side view of type c, inlet is located on the ramp; and the rest of the engine parallel to the airframe axis.**

ramp and the parallel surface. The inlet is located on the ramp with downstream engine components parallel to the airframe axis.[9–12]

The airflow conditions at the entrance of the engine have been investigated with several airframe configurations,[13,14] but they were not related to the engine performance. The effect of the integration of the scramjet engine into the airframe on engine performance and on payload of the aerospace plane has not been discussed sufficiently. In the present study, airframe-integrated scramjet inlet models were experimentally investigated in a Mach 4 wind tunnel to obtain characteristics of the three types of the integration. Then, based on the experimental results, simulations of the scramjet engine and the flight of the single-stage-to-orbit (SSTO) aerospace plane were conducted with simplified models to evaluate the influence of the integration form on the engine performance and the payload.

## Inlet Models Experiments

The characteristics of each integration form were investigated in the experiments with the scramjet inlet models. In the type b configuration, the expansion fan from the rear corner enters the inlet, and as a result, the flowfield inside the inlet is highly distorted and unpredictable. Modeling the capture of the expansion fan from the airframe ramp was one of the major subjects of the tests.

### Experimental Apparatus

*Wind Tunnel*

Experiments were conducted in a Mach 4 blowdown wind tunnel with a rectangular test section of 100 × 110 mm (Ref. 15). The total pressure and the total temperature were 2.2 MPa and 285 K, respectively. The duration of a test was 20 s, sufficiently long to measure multiple wall pressures with two mechanical pressure scanners (Scanivalves®). The unit Reynolds number was $1.2 \times 10^8$ m$^{-1}$.

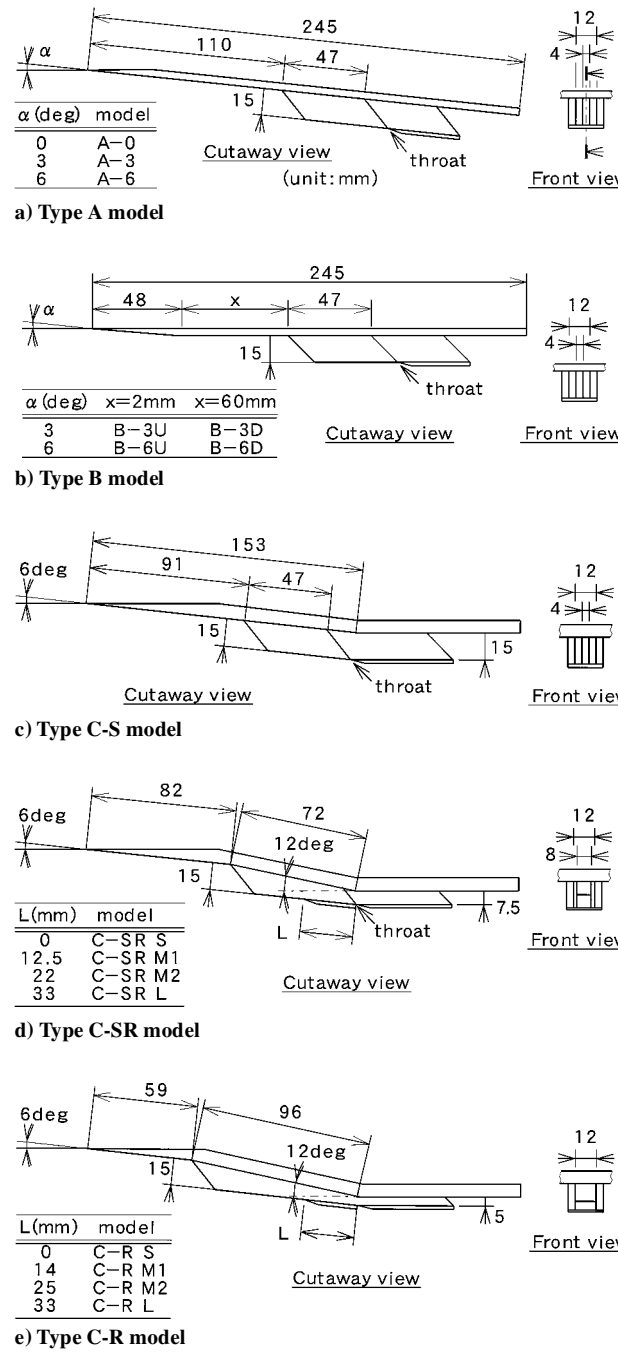


**Fig. 2 Schematic diagrams of the airframe-integrated inlet models.**

*Airframe-Integrated Inlet Models*

Figures 2a –2e show the models used in the present experiments. Each model consisted of a pair of side walls, a top wall, and a cowl. The top wall plate simulated the windward surface of the vehicle and was installed at the midheight of the wind tunnel. The top plate spanned the entire wind tunnel. The frontal area at the inlet entrance, which projected to a plane normal to the top wall surface, was 15 × 12 mm in all models. The side wall had a sweptback angle of 45 deg. The overall geometrical contraction ratio, which is the ratio of the cross section at the entrance to that at the exit of the inlet, was 3. The cowl leading edge was located at the end of the convergent section of the inlet, except in several cases of type C-SR and type C-R models. Downstream of the convergent section, there was a constant cross section duct part, which simulated an isolator. In this study, 16 models, each with a different geometry, were tested.

Type A models, which corresponded to type a in Fig. 1, had a flat top wall with inclination angles of 0, 3, or 6 deg. These three

angles were employed to evaluate the quantitative nature of the inlet performance. Each configuration was designated by combining an inclination angle and the model type, such as type A-3 (Fig. 2a). The inlet employed only side-wall compression.

The top plate of type B models had a wedge at the leading edge, which simulated the ramp. The model was attached downstream of the ramp, where the surface was parallel to the wind-tunnel axis. These models corresponded to type b in Fig. 1. The ramp angle was 3 or 6 deg. Side walls were the same as those of type A, and the entrance of the inlet models was located 2 mm downstream (U) or 60 mm downstream (D) of the end of the ramp. Each model was defined by the model type and the ramp angle followed by U or D, for example, type B-3D. In the models B-3D and B-6D, the cowl leading edge was located sufficiently downstream so as not to ingest the expansion fan from the corner of the top wall ramp end. In the models B-3U and B-6U, part of the expansion fan went inside the inlet. By the comparison of these four type B models, the effect of expansion-fan ingestion on the inlet performance was investigated, as well as the effect of the ramp angle.

In type C models, the top wall had a ramp followed by the parallel surface. The turning angle was 6 deg. Because the models straddled over the ramp and the parallel surface, the airflow was turned by the shock wave from the leading edge of the cowl and the expansion fan from the corner of the ramp. The models corresponded to type c in Fig. 1. In this type, with the same geometrical contraction ratio of 3, three models were prepared to compare the compression process: type C-S model employed only side-wall compression, type C-SR model employed both side-wall compression with a contraction ratio of 1.5 and ramp compression with a contraction ratio of 2, and type C-R model employed only ramp compression (Figs. 2c–2e). The top walls of the types C-SR and C-R models had a 6-deg second ramp inside the inlet, which started at the leading edge of the inlet. Four cowls with different lengths were prepared for the types C-SR and C-R models to reduce extra spillage caused by the shock wave from the second ramp. These cowls were referred by the designations S, M-1, M-2, and L, and their lengths are described in the caption of Fig. 2.

*Instrumentation*

Pressure holes were bored: 22–28 on the centerline of the top wall, 2–8 on the side walls, and 3 on the centerline of the cowl were also tapped. The diameter of each hole was 0.7 mm. In the constant cross section duct part, that is, the isolator, pitot pressures were measured at 5–12 points in a cross section. The inner and the outer diameters of the pitot tube were 0.3 and 0.6 mm, respectively. Wall pressure was measured with a 50-psia pressure transducer, and the pitot pressure was 200 psia. Accuracy of the wall-pressure measurement system was ±0.5%. Because of the difficulty of determining the flow direction inside the models, the flow static pressure was linearly interpolated from the wall pressures on both sides at the same lateral location. With this interpolated pressure and the measured pitot pressure, the local flow properties, for example, total pressure, were evaluated.

During the wind-tunnel operation, the shadowgraph image of the flowfield outside the inlet was observed for all of the models with a charge-coupled device video camera. It was confirmed that the shock wave from the top wall leading edge did not interact with the flowfield around the inlet models.

**Experimental Results and Discussion**

Figures 3a–3f show the wall-pressure distributions on the centerline of the top wall. In Figs. 3e and 3f, the effect of the cowl length is shown. Table 1 summarizes the experimental results of the mass capture ratio (CR), the total pressure efficiency $\eta_{\mathrm{Pt}}$, kinetic energy efficiency $\eta_{\mathrm{KE}}$, and the area-averaged Mach number in the isolator. In Table 1, the subscripts total and inlet indicate inclusion and exclusion of the precompression effect by the top wall, respectively. The definitions of the coefficients and the efficiencies are as follows:

$$\mathrm{CR}_{\mathrm{total}} = \frac{\int \rho_2 u_2 \,\mathrm{d}A}{\int \rho_{\mathrm{ref}} u_{\mathrm{ref}} \,\mathrm{d}A} = \frac{(\text{air mass flow rate in the isolator})}{(\text{air mass flow rate at the reference condition})} \tag{1}$$

$$\mathrm{CR}_{\mathrm{inlet}} = \frac{\int \rho_2 u_2 \,\mathrm{d}A}{\int \rho_1 u_1 \,\mathrm{d}A} = \frac{(\text{air mass flow rate in the isolator})}{(\text{air mass flow rate at the entrance of the model})} \tag{2}$$

$$\eta_{\mathrm{Pt,total}} = \frac{\int P_{t,2}\rho_2 u_2 \,\mathrm{d}A \Big/ \int \rho_2 u_2 \,\mathrm{d}A}{\int P_{t,\mathrm{ref}}\rho_{\mathrm{ref}} u_{\mathrm{ref}} \,\mathrm{d}A \Big/ \int \rho_{\mathrm{ref}} u_{\mathrm{ref}} \,\mathrm{d}A} = \frac{(\text{mean total pressure weighted by mass flow rate in the isolator})}{(\text{total pressure weighted by mass flow rate at the reference condition})} \tag{3}$$

$$\eta_{\mathrm{Pt,inlet}} = \frac{\int P_{t,2}\rho_2 u_2 \,\mathrm{d}A \Big/ \int \rho_2 u_2 \,\mathrm{d}A}{\int P_{t,1}\rho_1 u_1 \,\mathrm{d}A \Big/ \int \rho_1 u_1 \,\mathrm{d}A} = \frac{(\text{mean total pressure weighted by mass flow rate in the isolator})}{(\text{mean total pressure weighted by mass flow at the entrance of the model})} \tag{4}$$

**Table 1 Performance of inlet models**

| Model | $M_2$ | $\rho_2 u_2$ | $\mathrm{CR}_{\mathrm{inlet}}$ | $\mathrm{CR}_{\mathrm{total}}$ | $\eta_{\mathrm{Pt\,inlet}}$ | $\eta_{\mathrm{Pt\,total}}$ | $\eta_{\mathrm{KE\,inlet}}$ | $\xi$ |
|---|---|---|---|---|---|---|---|---|
| A-0 | 2.48 | 862.2 | 0.674 | 0.674 | 0.591 | 0.591 | 0.953 | 3.9 |
| A-3 | 2.28 | 1064.5 | 0.676 | 0.832 | 0.613 | 0.611 | 0.951 | 5.6 |
| A-6 | 2.13 | 1240.8 | 0.613 | 0.970 | 0.639 | 0.626 | 0.950 | 7.3 |
| B-3D | 2.38 | 897.3 | 0.714 | 0.701 | 0.626 | 0.624 | 0.958 | 4.7 |
| B-6D | 2.53 | 964.3 | 0.792 | 0.754 | 0.585 | 0.572 | 0.952 | 4.4 |
| B-3U | 2.66 | 891.2 | —— | 0.696 | 0.593 | 0.591 | 0.953 | 3.6 |
| B-6U | 2.55 | 813.3 | —— | 0.636 | 0.561 | 0.550 | 0.948 | 3.6 |
| C-S | 1.90 | 1232.7 | 0.610 | 0.963 | 0.430 | 0.421 | 0.900 | 8.7 |
| C-SR S | 2.40 | 1081 | 0.535 | 0.845 | 0.666 | 0.652 | 0.955 | 5.3 |
| C-SR M1 | 2.16 | 1461.9 | 0.723 | 1.142 | 0.601 | 0.589 | 0.943 | 8.4 |
| C-SR M2 | 1.94 | 1567.8 | 0.775 | 1.225 | 0.542 | 0.531 | 0.930 | 11.4 |
| C-SR L | 1.63 | 1866.6 | 0.923 | 1.459 | 0.537 | 0.525 | 0.929 | 15.1 |
| C-R S | 2.24 | 662 | 0.327 | 0.517 | 0.273 | 0.267 | 0.836 | 4.1 |
| C-R M1 | 2.37 | 1164 | 0.576 | 0.910 | 0.539 | 0.528 | 0.929 | 6.4 |
| C-R M2 | 1.92 | 1188 | 0.588 | 0.928 | 0.363 | 0.355 | 0.877 | 9.5 |
| C-R-L | 1.89 | 1408.1 | 0.696 | 1.100 | 0.450 | 0.441 | 0.906 | 10.8 |

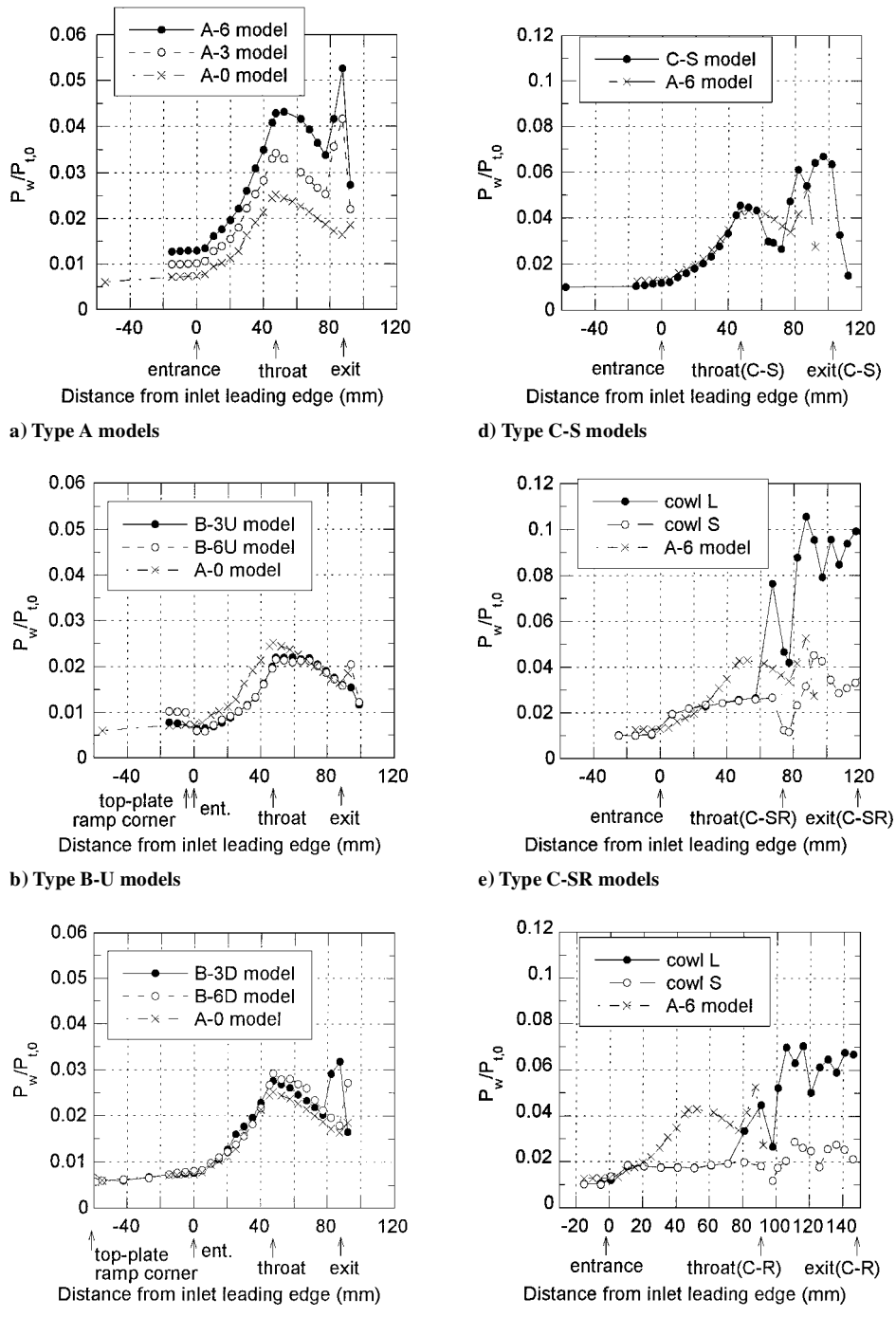


**Fig. 3 Wall pressure distributions on the centerline of the top wall.**

The properties at the reference condition were substituted by those obtained at the entrance of the type A-0 model, that is, the averaged values of 15 × 12 mm area at the inlet entrance, including the boundary layer on the plate. Here, $\xi$ is the ratio of the area-weighted average of the top wall pressure in the isolator to the free stream static pressure. This represents a mean pressure ratio of the inlet model. The characteristics of each model are now discussed.

*Type A Models*

$CR_{total}$ and $\xi$ were improved as the inclination angle increased (Table 1 and Fig. 3a). $CR_{inlet}$ became slightly lower because of the reduction of the entrance Mach number due to the stronger shock wave from the leading edge of the top wall. With reduction of the Mach number, spillage from the open bottom increased due to the effect of the sweptback geometry.[2] With the larger inclination angle, $\eta_{Pt,total}$ also showed a slight increase. The increase of the top wall angle diminished the top wall boundary-layer thickness. The measured heights of the boundary layer of 99% primary flow velocity at the inlet entrance of the models A-0, A-3, and A-6 were 4.2, 3.8, and 2.8 mm, respectively. The reduction of the fraction of the boundary layer to the entire flow captured by the inlet resulted in better total pressure efficiency. The kinetic energy efficiency was evaluated from the experiments, and no substantial difference was found between the models.

From the viewpoint of the advantage of precompression and the mass capture, the inlet should be installed on the ramp portion of the airframe windward surface. The larger inclination angle of the top wall plate resulted in better performances within the range of the present experimental conditions.

*Type B Models*

These models virtually canceled out the precompression effect. In spite of the existence of a ramp of 3 or 6 deg, both $CR_{total}$ and $\eta_{Pt,total}$ were almost equal to those of model A-0. The pressure ratio also became compatible with model A-0. The relative position of the inlet to the ramp corner did not result in a significant change in the performance. Thus, in the simulation for type b, the airflow was assumed to enter the inlet after it went through the entire expansion wave. This configuration did not receive any advantage from the precompression.

*Type C Models*

This configuration attained sufficient mass capture. $CR_{total}$ of the type C-S model was as high as that of the type A-6 model, and $\xi$ was better than that of the type A-6 model. On the other hand, $\eta_{Pt,total}$ became lower than that of model A-6. In the type C-SR model, $\xi$ and $CR_{total}$ became higher as the cowl was extended upstream. These values were equal to or greater than those of model A-6, when the cowl was extended sufficiently. The cowl extension caused no significant reduction in $\eta_{Pt,total}$. In the type C-R model, with the extended cowl, $CR_{total}$ was as high as that of model A-6 and $\xi$ increased. On the other hand, $\eta_{Pt,total}$ of the model C-R S became significantly lower than that of model A-6 caused by larger spillage of the primary flow.

The precompression effect was attained in the type A and type C models. In the type B models, the precompression effect was lost. In the type B models, there was no difference in the inlet performance due to relative position of the inlet to the ramp corner. Although the models showed different characteristics in performance, most of the type A, type B, and type C-SR models showed similar values in $\eta_{KE,inlet}$ and $CR_{inlet}$.

## Simulations of Scramjet Engine and Flight of the SSTO Aerospace Plane

In this section, based on the experimental results, differences in the scramjet engine performance and differences in payload of the aerospace plane due to variations in engine–airframe integration are examined. In actual flight, several types of engines or engine modes are used to match the velocity region. However, in this study, the effect of the engine–airframe integration is considered only in the scramjet-operating regime, where the precompression affects the engine performance significantly.

### Integration of Scramjet Engine into Airframe

Three airframe integration configurations, that is, types a, b, and c, were examined (Fig. 1). All of the airframes had a two-dimensional, sharp-wedge nose, and their length, width, and the windward surface wedge angle from the airframe axis were 80 m, 15 m, and 3 deg, respectively. The angle of the external nozzle was different in each model.

In type a, the shock from the forebody nose impinged on the leading edge of the cowl at the flight Mach number of 12. In type b, the upstream part of the forebody was the same as that of type a, but the ramp was terminated and the vehicle surface was parallel to the airframe axis just upstream of the scramjet engine. As was confirmed by the experiments, it was assumed that the precompressed air passed through the entire expansion fan from the corner of the airframe before it entered the engine. In type c, the scramjet engine was aligned with the airframe axis. However, the cowl was extended forward to capture the same mass flow rate as that of type a. The airflow was turned toward the airframe axis by the shock wave from the cowl.

### Calculation Methods

*Scramjet Engine Performance*

The scramjet engine performance was calculated with the quasi-one-dimensional flow method. The air entering the engine passed a planar shock wave generated by the forebody, which was calculated with the two-dimensional oblique shock wave relations. The end effect at both sides of the forebody[16] was neglected for the sake of simplicity. In the calculation of the engine performance, the angle of attack, that is, the angle between the freestream direction and airframe axis, was fixed to be 3 deg.

The airflow condition into the inlet was calculated for each integration type, and $CR_{inlet}$ was assumed to be 1.0, that is, no spillage from the inlet. The effect of the boundary layer on the airframe surface on engine performance was not considered. The inlet performances were calculated with $\eta_{KE,inlet}$ of 0.98, which was deduced from an empirical equation.[17] According to the experiments, there was no significant difference in $\eta_{KE,inlet}$ between the three types of the inlet models. The geometrical contraction ratio was 5. From Mach 6 to 8, the amount of fuel was adjusted so that the Mach number of the combustion gas in the constant cross section duct was just above unity to avoid thermal choking. From flight Mach numbers 8 to 12, the stoichiometric hydrogen fuel was vertically injected in the constant cross section duct, and the fuel was assumed to react completely. In the internal nozzle, the combustion gas expanded isentropically and one dimensionally with an expansion area ratio of 5. In the external nozzle, the combustion gas expanded through a two-dimensional expansion wave.

Both air and the combustion gas were calorically and thermally ideal. The ratios of the specific heats were 1.40 for air and 1.25 for the combustion gas, respectively, and the molecular weight of the combustion gas was 24.7. These properties of the combustion gas were calculated with a code[18] in the equilibrium condition. The heat release at combustion by hydrogen was $121 \times 10^3$ kJ/1-kg hydrogen.

The engine internal thrust was calculated as follows. First, the difference of the impulse functions between the inlet entrance and the internal nozzle exit was calculated. This was designated as the inviscid thrust. Then, the friction drag of the internal surface was estimated and was subtracted from the inviscid thrust to obtain the internal thrust. The total thrust was defined as the sum of the engine internal thrust and force/drag on the windward airframe surface, including forebody, aftbody, and cowl of the engine module. The friction coefficient was set to be 0.0025 on the entire surface.[19]

*Payload Estimation*

The effect of the airframe–scramjet integration on payload was estimated by a flight simulation of a SSTO aerospace plane to a 100-km low Earth orbit. The aerodynamic data of the plane, the other engine performances, and the weights of the vehicle components were the same as those used in a previous investigation.[20] The gross takeoff mass was 460 Mg.

From takeoff to Mach 6, the air-turboramjet (ATR) operated. The projected cross section of the ATR modules was 15 $m^2$ at the entrance. The equivalence ratio of the ATR was unity. The specific impulse of the ATR calculated by Sakata et al.[21] was used. The scramjet operated from Mach 6 to Mach 12. The projected cross section of the scramjet was 30 $m^2$. After operation of the scramjet, the rocket engine took over to carry the vehicle into orbit. The maximum total thrust of the rocket engine was 4060 kN, and the specific impulse was 4018 $m \cdot s^{-1}$ at the sea level. Propellants were hydrogen and oxygen. The trajectory of the aerospace plane was within the two-dimensional plane.

### Results of the Simulation and Discussion

*Scramjet Engine Performance*

The calculated performances of the three types of airframe-integrated scramjet engines are shown in Figs. 4 and 5. Figure 4a shows the air mass flow into the engine. This quantity is nondimensionalized by the product of the mass flux of the freestream and the projected cross-sectional area at the engine entrance. In all of the models, the mass flow rates were larger than unity due to the precompression by the angle of attack. In types a and c, this was also due to the airframe ramp. The mass flow rate of type b was smaller than those of types a and c. The mass flux of type b decreased due to the expansion fan in front of the engine. The mass capture was about 80% that of type a or type c at Mach 4. In the experiments with the same inlet model, $CR_{total}$ of type B was about 0.7, and that

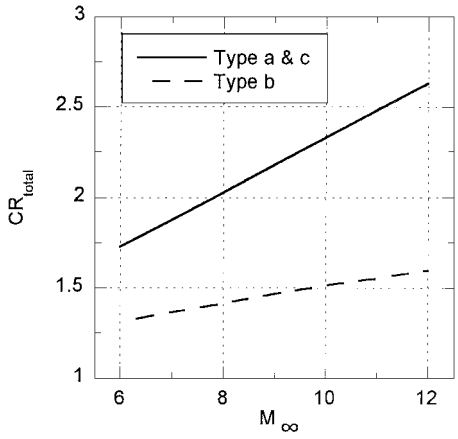


a)

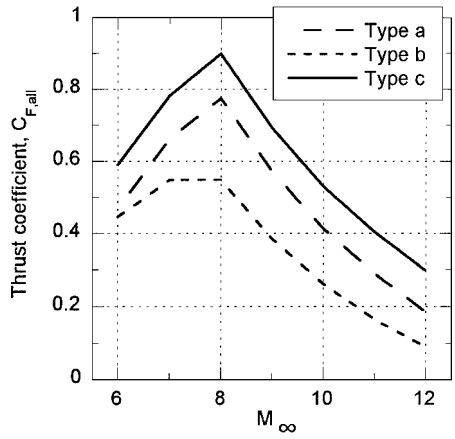


b)

**Fig. 4 Calculation results: a) mass capture ratio; b) thrust coefficient with the engine thrust and the drag of the windward surface of the airframe.**

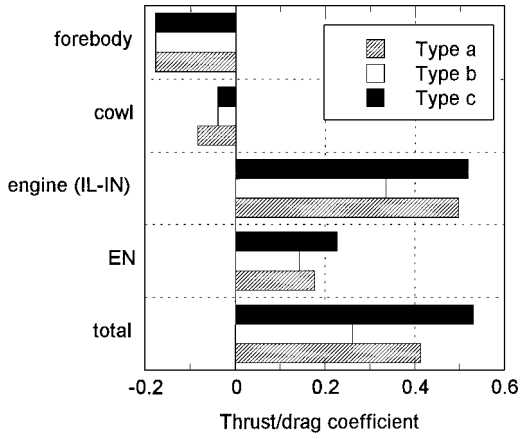


**Fig. 5 Breakdown of the thrust coefficients at the flight Mach number of 10.**

of type A-6 was 0.970. The ratio obtained experimentally showed reasonably good agreement with calculations.

Figure 4b shows the thrust coefficient of the engine, defined as the ratio of the total thrust to the product of the flight dynamic pressure and the projected cross-sectional area of the engine entrance. Type c delivered the largest total thrust coefficient, and type a was the second largest. Suffering from its smaller air mass flow rate, type b had a significantly lower thrust coefficient than the others. The specific impulses of the engines were not significantly different between types a, b, and c because there was no difference in the total enthalpy of the unit mass of the combustion gas in the stoichiometric condition. The primary reason for the engine thrust difference was the difference in air mass flow or the air impulse function into the engine, as was also observed in the experiments. The difference in the thrust coefficients became larger in the high Mach number regime, where the difference of the mass capture ratios increased.

Beside the decrease of the air mass flow into the engine, the decrease of the thrust was also caused by inadequacy in the airframe and the engine configurations. Figure 5 shows a breakdown of the thrust coefficients at the flight Mach number of 10. The difference in the thrust coefficient between type a and type c was due to the differences in the external nozzle thrust and the cowl drag in addition to the engine internal thrust. As for the internal thrust, type a had a disadvantage because the direction of engine thrust was not aligned to the airframe axis.

As shown in Fig. 1, the divergence angle of the external nozzle of type a was larger than that of type c. The further expansion of the combustion gas in the external nozzle of type a resulted in lower wall pressure and smaller thrust than that of type c, even though the projected area of the external nozzle became larger than that of type c. The cowl drag of type b or type c was smaller than that of type a because the cowl outer surface is parallel to the airframe axis, and thus, the pressure drag was small.

**Table 2 Contents of mass of aerospace plane (unit: Mg)**

| Item | Model | | |
|---|---|---|---|
| | Type a | Type b | Type c |
| Propellant | | | |
| Fuel (ATR) | 40.5 | 40.5 | 40.5 |
| Fuel (scramjet) | 86.1 | 100.4 | 54.4 |
| Fuel (rocket) | 30.8 | 29.5 | 33.9 |
| Oxygen | 184.9 | 177.1 | 203.2 |
| Total propellants | 342.3 | 347.5 | 332.0 |
| Tank | | | |
| Hydrogen | 17.6 | 19.0 | 14.5 |
| Oxygen | 3.1 | 3.0 | 3.4 |
| Total tanks | 20.7 | 22.0 | 17.9 |
| Airframe and engines | 91.1 | 91.1 | 91.1 |
| Payload | 5.9 | −0.6 | 19.0 |
| Total initial mass | 460.0 | 460.0 | 460.0 |

*Payload Estimation of the SSTO Aerospace Plane*

Table 2 lists the contents of the mass ratios of the aerospace plane in the payload estimation. The payload of type a was 5.9 Mg, whereas that of type c was 19.0 Mg. The operating time and the consumed fuel of type a were larger than those of type c because of the lower thrust. The difference in the engine and the airframe configurations caused the large difference in the payload.

Type b could not produce sufficient thrust during the scramjet engine operation, and thus, the calculated payload became negative. The engine ingested a smaller amount of airflow and delivered lower thrust than the other types due to the inadequacy of the integration form of the engine into the airframe. Based on these results, type b configuration should be avoided.

As a result, the inlet should be installed on the ramp to inhale the precompressed air, but the section downstream of the inlet entrance should be turned parallel to the airframe axis to reduce the cowl drag and to increase the thrust at the external nozzle.

## Conclusions

The effects of the configuration of the scramjet integration into the airframe on the engine performance and the payload were investigated. The inlet performances were experimentally studied in several configurations, and the effect of the integration forms on the scramjet performance and the payload of the SSTO plane were calculated using simple models. The investigation clarified the following points.

1) When the inlet was integrated on the ramp surface of the airframe, as in the type A model, a larger ramp angle resulted in better performances in mass capture ratio and pressure ratio within the

conditions tested. However, the pressure drag on the cowl increased and the thrust at the external nozzle decreased. Thus, the payload decreased.

2) When the inlet was attached to the airframe surface parallel to the axis, the precompression effect was neutralized. The effect of the neutralization was observed even when the inlet model was located just downstream of the ramp corner. The air mass flow into the engine decreased, and the engine could not develop sufficient thrust for SSTO applications.

3) In the case in which the inlet entrance was attached to the airframe ramp surface with subsequent engine components parallel to the airframe axis, the engine showed the best performance. With this configuration, the precompressed air was effectively swallowed, cowl drag was reduced, and thrust at the external nozzle was increased. The payload was the largest for this configuration in the present study.

## Acknowledgments

The authors acknowledge the assistance of Yoshinori Futonagane, Yusuke Oikawa, and Tomoyuki Abe, former graduate and undergraduate students of Tohoku University, in conducting the experiments.

## References

[1]Heiser, W. H., Pratt, D. T., Daley, D. H., and Mehta, U. B., *Hypersonic Airbreathing Propulsion*, AIAA Education Series, Washington, DC, 1994, pp. 24–26.

[2]Trexler, C. A., and Sounders, S. W., "Design and Performance at a Local Mach Number of 6 of an Inlet for an Integrated Scramjet Concept," NASA TN D-7944, Aug. 1975.

[3]Nomura, S., Hozumi, K., Kawamoto, I., and Miyamoto, Y., "Experimental Studies on Aerodynamic Characteristics of SSTO Vehicle at Subsonic to Hypersonic Speeds," *Proceedings of the 16th International Symposium on Space Technology and Science*, the Japan Society for Aeronautical and Space Sciences, Tokyo, 1988, pp. 1547–1554.

[4]Wilhite, A. W., Engelund, W. C., Stanley, D. O., Neftel, J. C., Lepsch, R. A., Bush, L. B., and Wurster, K. E., "Technology and Staging Effects on Two-Stage-to-Orbit Systems," *Journal of Spacecraft and Rockets*, Vol. 31, No. 1, 1994, pp. 31–38.

[5]Maita, M., Miyajima, H., and Mori, T., "System Studies on Space Plane Powered by Scram/LACE Propulsion System," AIAA Paper 92-5024, Dec. 1992.

[6]Bertin, J. J., Towne, M. C., Malan, M. A., Kreins, A. F., Zuber, M. E., and Parks, M. B., "Viscous/Inviscid Interactions of the Forebody Flowfield of an Airbreathing Hypersonic Vehicle," *Journal of Spacecraft and Rockets*, Vol. 35, No. 4, 1998, pp. 442–449.

[7]Freeman, D. C., Talay, T. A., Stanley, D. O., Lepsch, R. A., and Wilhite, A. W., "Design Options for Advanced Manned Launch Systems," *Journal of Spacecraft and Rockets*, Vol. 32, No. 2, 1995, pp. 241–249.

[8]Leingang, J. L., Maurice, L. Q., and Carreiro, L. R., "In-Flight Oxidizer Collection Systems for Airbreathing Space Boosters," *Developments in High-Speed-Vehicle Propulsion Systems*, Progress in Astronautics and Aeronautics, AIAA Reston, VA, 1996, pp. 333–384.

[9]Ikawa, H., "Rapid Methodology for Design and Performance Prediction of Integrated Supersonic Combustion Ramjet Engine," *Journal of Propulsion and Power*, Vol. 7, No. 3, 1991, pp. 437–444.

[10]Heiser, W. H., Pratt, D. T., Daley, D. H., and Mehta, U. B., "Hypersonic Airbreathing Propulsion," AIAA Education Series, AIAA, Washington, DC, 1994, pp. 198–201.

[11]Huebner, L. D., "Computational Inlet-Fairing Effects and Plume Characterization on a Hypersonic Powered Model," *Journal of Aircraft*, Vol. 32, No. 6, 1995, pp. 1240–1245.

[12]Bogar, T. J., Alberico, J. F., Johnson, D. B., Espinosa, A. M., and Lockwood, M. K., "Dual-Fuel Lifting Body Configuration Development," AIAA Paper 96-4592, Nov. 1996.

[13]Berens, T. M., and Bissinger, N. C., "Forebody Precompression Effect and Inlet Entry Condition for Hypersonic Vehicles," *Journal of Spacecraft and Rockets*, Vol. 35, No. 1, 1998, pp. 30–36.

[14]Ide, H., Armstrong, J., Szema, K. Y., and Haney, J., "Hypersonic Vehicle Forebody Design Studies and Aerodynamic Trends," AIAA Paper 89-2182-CP, 1989.

[15]Kanda, T., Komuro, T., Masuya, G., Kudo, K., Murakami, A., Tani, K., Wakamatsu, Y., and Chinzei, N., "Mach 4 Testing of Scramjet Inlet Models," *Journal of Propulsion and Power*, Vol. 7, No. 2, 1991, pp. 275–280.

[16]Tani, K., Kanda, T., Kudo, K., and Akihisa, D., "Effect of Sides-Spillage from Airframe on Scramjet Engine Performance," *Journal of Propulsion and Power*, Vol. 17, No. 1, 2001, pp. 139–145.

[17]Heiser, W. H., Pratt, D. T., Daley, D. H., and Mehta, U. B., *Hypersonic Airbreathing Propulsion*, AIAA Education Series, AIAA, Washington, DC, 1994, p. 225.

[18]Svehla, R. A., and McBride, B. J., "FORTRAN IV Computer Program for Calculation of Thermodynamic and Transport Properties of Complex Chemical Systems," NASA TN D-7056, Jan. 1973.

[19]Swithenbank, J., "Hypersonic Airbreathing Propulsion," *Progress in Aeronautical Sciences*, edited by D., Küchemann, Vol. 8, Pergamon, Oxford, 1967, p. 245.

[20]Kanda, T., and Kudo, K., "Payload to Low Earth Orbit by Aerospace Plane with Scramjet Engine," *Journal of Propulsion and Power*, Vol. 13, No. 1, 1996, pp. 164–166.

[21]Sakata, K., Yanagi, R., Shindo, S., Minoda, M., and Nouse, H., "Conceptual Study on Air-Breathing Propulsion for Space Plane," *Proceedings of the 16th International Symposium on Space Technology and Science*, the Japan Society for Aeronautical and Space Sciences, Tokyo, 1988, pp. 107–112.